THE JOURNAL OF BIOLOGICAL CHEMISTRY VOL. 287, NO. 26, pp. 22030–22042, June 22, 2012

Matrix Disruptions, Growth, and Degradation of Cartilage with Impaired Sulfation*[S]

Received for publication, February 22, 2010, and in revised form, April 23, 2012 Published, JBC Papers in Press, May 3, 2012, DOI 10.1074/jbc.M110.116467

Edward L. Mertz[‡1], Marcella Facchini[§], Anna T. Pham[‡], Benedetta Gualeni[§], Fabio De Leonardis[§], Antonio Rossi[§], and Antonella Forlino[§]

From the [‡]Section on Physical Biochemistry, Eunice Kennedy Shriver NICHD, National Institutes of Health, Bethesda, Maryland 20892 and the [§]Department of Molecular Medicine, University of Pavia, Section of Biochemistry, Pavia 27100, Italy

Background: Mutations in chondrocyte sulfate transporter cause dwarfism and joint degradation.
Results: The resulting chondroitin undersulfation and collagen disorientation disrupt the protective articular surface and correlate with the chondroitin synthesis rate across epiphyseal cartilage.
Conclusion: Matrix synthesis accelerates in enlarging chondrocytes, increasing their susceptibility to matrix-related mutations.
Significance: Findings elucidate mechanisms of sulfation disorders, orientation of matrix collagen, and bone elongation.

Diastrophic dysplasia (DTD) is an incurable recessive chondrodysplasia caused by mutations in the SLC26A2 transporter responsible for sulfate uptake by chondrocytes. The mutations cause undersulfation of glycosaminoglycans in cartilage. Studies of *dtd* mice with a knock-in *Slc26a2* mutation showed an unusual progression of the disorder: net undersulfation is mild and normalizing with age, but the articular cartilage degrades with age and bones develop abnormally. To understand underlying mechanisms, we studied newborn *dtd* mice. We developed, verified and used high-definition infrared hyperspectral imaging of cartilage sections at physiological conditions, to quantify collagen and its orientation, noncollagenous proteins, and chondroitin chains, and their sulfation with 6-μm spatial resolution and without labeling. We found that chondroitin sulfation across the proximal femur cartilage varied dramatically in *dtd*, but not in the wild type. Corresponding undersulfation of *dtd* was mild in most regions, but strong in narrow articular and growth plate regions crucial for bone development. This undersulfation correlated with the chondroitin synthesis rate measured via radioactive sulfate incorporation, explaining the sulfation normalization with age. Collagen orientation was reduced, and the reduction correlated with chondroitin undersulfation. Such disorientation involved the layer of collagen covering the articular surface and protecting cartilage from degradation. Malformation of this layer may contribute to the degradation progression with age and to collagen and proteoglycan depletion from the articular region, which we observed in mice already at birth. The results provide clues to *in vivo* sulfation, DTD treatment, and cartilage growth.

Sulfated molecular species like glycosaminoglycan (GAG)[2] chains of proteoglycans, cholesterol, lipids, xenobiotics *etc.* provide numerous structural and signaling functions vital for many tissues. In cartilage, sulfated GAGs also provide tissue swelling and elasticity requiring sulfated GAGs in enormous quantities. This requirement makes cartilage and bone developing from cartilage particularly susceptible to genetic disruptions of the sulfation pathway, resulting in recessive chondrodysplasias in humans (1–4) and mice (5–10). Because such disruptions may affect cell functions, extracellular matrix, and whole limbs at multiple levels, genotype-phenotype relationships are still poorly understood, complicating development of cures.

Diastrophic dysplasia (DTD) was the first human chondrodysplasia with impaired sulfation whose genetic defect was identified (1). The mutations are in the SLC26A2 sulfate/chloride antiporter (also called DTD sulfate transporter) responsible for inorganic sulfate uptake by chondrocytes. The mutations cause GAGs undersulfation, bone malformations, and joint degradation (11–14). Single nucleotide polymorphisms in *SLC26A2* also associate with systemic-onset juvenile idiopathic arthritis (15). The key features of human DTD have been reproduced in a *dtd* mouse with knocked-in A386V mutation originally found in a patient (8, 16, 17).

The *dtd* mouse reveals an unusual progression for genetic disorders. A primary biochemical defect, net undersulfation of chondroitin, which is the dominating sulfated species of cartilage, is slightly below normal at birth (0.7 sulfate/disaccharide in *dtd versus* 0.9 in wild type) and approaches normal values with age (8). Conversely, *dtd* mice have barely detectable clinical phenotype at birth and develop skeletal abnormalities and severe articular cartilage degradation by 2 months, similar to young human adults (8, 18).

In this work, we focused on primary defects associated with extracellular matrix. We studied epiphyseal cartilage of the *dtd*

* This work was supported, in whole or in part, by the National Institutes of Health Director's Challenge Fund, the NICHD Intramural Research Program, PRIN 20094C2H2M, Regione Lombardia REGLOM16, and European Community FP6 EuroGrow Grant LSHM-CT-2007-037471.
[S] This article contains supplemental Materials, Figs. S1–S10, and Tables S1 and S2.
[1] To whom correspondence should be addressed: NIH, 9000 Rockville Pike, Bldg. 9, Rm. 1E125, Bethesda, MD 20892. Fax: 301-402-0292; E-mail: mertze@mail.nih.gov.

[2] The abbreviations used are: GAG, glycosaminoglycan; DTD, diastrophic dysplasia; HDIR, high-definition infrared; NCP, noncollagenous core proteins; PAPS, 3′-phosphoadenosine 5′-phosphosulfate; C0S, unsulfated chondroitin; C4S, chondroitin-4-sulfate; C6S, chondroitin-6-sulfate.

mouse at birth when mechanical loads and their secondary effects on degradation of undersulfated cartilage should be negligible. We examined all regions between the articular surface and the mineralizing front of the epiphyseal cartilage. At birth, these regions are continuous hyaline cartilage. Yet, they are involved in different functions of articular cartilage development, preparation for subchondral bone formation, and longitudinal bone growth, all of which are abnormal in DTD (18).

As in many disorders compatible with life, early *dtd* abnormalities are mild, but may vary across functionally different regions separated by a few tens of micrometers. Such spatial resolution is not easily achievable by existing quantitative techniques, whereas mild defects are difficult to track by conventional histology.

To track mild defects, we advanced infrared (IR) hyperspectral imaging, which detects chemical groups via their characteristic peaks in the IR absorption spectra recorded with micrometer spatial resolution (see Refs. 19–23 for previous applications to cartilage). Samples for this technique are usually dehydrated to eliminate strong absorption of IR light by water. However, the dehydration distorts the tissue and macromolecular structure and introduces multiple nonphysiological interactions between collapsed macromolecules, smearing spectral peaks (24) and reducing the number of resolved molecular components. We used a specially designed chamber with thermomechanical stabilization of spectral distortions in sections maintained in physiological-like solution (25, 26). Combining this setup with spectral analysis based on purified and characterized model compounds, we devised a high-definition approach, which increased spectral reproducibility and the number of resolved molecular components, resulting in quantitative, label-free, "histological" images of multiple components from a single recording.

Using this new method and autoradiographic imaging of chondroitin synthesis, we found several extracellular abnormalities across functionally different cartilage regions. The findings provided insights into DTD, *in vivo* sulfation, orientation of matrix collagen, and bone elongation.

MATERIALS AND METHODS

This section outlines nonstandard methods. Supplemental Materials describes further details and standard techniques. Materials were bought from Sigma unless stated otherwise.

Animals

Newborn (0.5 day old) *dtd* mice with knocked-in homozygous A386V substitution in the *Slc26a2* gene (8) and their wild type (*wt*) and heterozygous littermates were used. The mice were inbred progeny of F1 generation of C57Bl/6J and 129/SV backgrounds, which provided full penetration of the *dtd* phenotype.

Autoradiography of [^{35}S]Sulfate Incorporation into Explants

Whole femurs were incubated in a medium with 33 μCi/ml of [^{35}S]sulfate and total inorganic sulfate concentration of 0.8 mM (similar to that in mouse serum) for 2 or 4 h at 37 °C and 5% CO_2. The explants were fixed in 2% formaldehyde solution and cryosectioned to 12 μm in the mid-coronal plane. The cryosections deposited onto glass slides were exposed on phosphoimaging screens, and autoradiographic and autofluorescence images of the sections were recorded with an FLA-5000 scanner (Fujifilm) with 25/50-μm nominal/actual spatial resolution. Visible transmission images of the sections with 0.5-μm resolution were also recorded with a microscope (Fig. 1). The radiographic, fluorescence, and transmission images were registered to within ~13 μm (confirmed via overlaid positions of thin radioactive debris on the slides). Cell positions at the transmission images were marked manually, and cell density and radiographic intensity profiles along the lines in Fig. 1 were evaluated using ImageJ software (NIH) (Fig. 1). The radiographic profiles were deconvoluted (to evaluate intensity near cartilage boundaries) and normalized by cell density.

High-definition Infrared Hyperspectral Imaging

Infrared hyperspectral imaging of cartilage composition in sections was performed in the "high definition" (HDIR) mode, in which accuracy and peak resolution, key factors in spectral analyses, were increased by advanced procedures for sample handling, spectra recording and analyses, and purification and characterization of model compounds. Advantages of our and previous analyses are compared in supplemental Materials.

Sample Handling

Proximal halves of the femurs were fixed mildly (1% formaldehyde in PBS for 4–8 h at 22 ± 2 °C), and 12-μm midcoronal cryosections were cut under a hard-tissue protocol. Sections were photographed to determine position of mineralizing cartilage and, then, demineralized in 0.5 M EDTA, pH 8.0, for 5 min. A section was placed between two 2-mm BaF_2 windows (avoiding section stretching) and mounted in a thermomechanically stabilized, flow-through chamber (25) and kept at 20 ± 0.1 °C. Sections were equilibrated with an excess of 2 mM $CaCl_2$, 150 mM NaCl, pH 7.5 ± 0.1 solution (CNC) flushed into the chamber. Model compounds solutions in CNC at pH 7–8 were flushed into a 4–6-μm gap between assembled windows or deposited as a 0.5-μl droplet before assembly, and kept at 20 ± 0.1 °C. CNC contained calcium to maintain BaF_2 windows passivation and prevent adsorption and decomposition of sulfated glycosaminoglycans by barium. CNC had no buffer to avoid its interfering spectral contributions. Constancy of pH of samples in CNC was confirmed.

Spectra Recording

IR absorption spectra of the samples were recorded with a Hyperion 3000 microscope attached to a Vertex 70 Fourier transform infrared spectrometer equipped with ×15, 0.4 NA objective and condenser, low-pass 3850 cm^{-1} filter, holographic ZnSe polarizer inserted before the sample, and focal plane 128 × 128 array of detectors (Bruker Optics). The spectra were collected with 4 cm^{-1} spectral resolution in the 820–3950 cm^{-1} range by averaging 1000 scans accumulated for 60 min. Several hardware precautions were made to increase spectra quality.

Model Compounds

Our spectral analysis was based on model compounds representing major components of cartilage extracellular matrix.

Model compounds were carefully selected, purified, and prepared at aggregation state and conditions resembling those of the cartilage sections.

Glycosaminoglycans—Model chondroitins, unsulfated (C0S), -4-sulfate (C4S), and -6-sulfate (C6S), were analyzed in detail, as these GAGs dominated in our samples. Several commercial chondroitins were analyzed by ion exchange high performance liquid chromatography (HPLC) (8) and three compounds were selected based on their purity (90–95%) and enrichment with a particular sulfated form (83–94%) (supplemental Table S1). Purity from low molecular weight compounds and residual buffer salts with interfering spectral contributions was confirmed by dialysis. Spectra of the selected chondroitins at ~2% concentrations were normalized by the IR light path length and decomposed onto individual C0S, C4S, and C6S components based on their HPLC determined concentrations. The individual spectra (Fig. 2*B*) were used to predict spectra of chondroitin compounds with lower enrichment (63–80%). The predicted and measured spectra agreed to within their purity (80–90%). Spectra of 0.5 and 2% solutions of hyaluronate from rooster comb and dermatan sulfate from porcine mucosa (Fig. 2*B*) were recorded "as is" because their content was small in our samples ("Results").

Collagen—Because of the limited quantity, purity, and calibration of mouse cartilage collagens, we used several collagen sources: pepsin-treated bovine type II (Elastin Products), a mixture of acid-soluble mouse type II and type I (Sigma), and mouse and rat type I from tail tendons. We removed impurities, degradation products, and proteoglycans from these samples by collagen precipitation induced by slow *in vitro* fibrilogenesis (26) (supplemental Materials). Purity (99%) and collagen types of these preparations were confirmed by electrophoresis, CNBr peptides, chondroitinase ABC digestion, and HDIR. The bovine type II collagen reconstituted into fibers (Fig. 2*A*) was found to be a suitable model for isotropic spectra of mouse type II collagen dominating in cartilage (supplemental Fig. S2 and Table S2). HDIR absorptivity and concentration of the model type II collagen were calibrated via HDIR and circular dichroism spectra of solutions of pepsin-treated rat type I collagen monomers (supplemental Fig. S2). This calibration was confirmed by HDIR measurement of the water volume fraction in the fibers. Spectra of the selected models represented the triple helical motif of most collagen types because this motif is conserved and constitutes almost entire collagen molecules.

Noncollagenous Core Proteins (NCP)—To model NCP, we purified from smaller molecules by dialysis proteoglycans decorin, biglycan, and aggrecan (PG) abundant in cartilage and a "garden variety" protein bovine serum albumin (BSA, 99% pure) (Fig. 2*A* and supplemental Fig. S3). We used several proteins because total mass of NCP in newborn cartilage matrix is not dominated by any particular protein: In agreement with data for bovine nasal cartilage (27), our HDIR analysis indicated that the measured mass ratio NCP/GAG ~ 0.5 was higher than NCP/GAG ~ 0.1 expected for aggrecan, which is the most abundant NCP and the main carrier of GAG chains (Fig. 4, *A* and *C*). After removing GAG contributions from the PGs spectra, we found that spectral characteristics of the PG cores and BSA were sufficiently similar and evaluated model NCP characteristics (supplemental Table S2). Concentrations of the cores and BSA were measured via integral intensities of the amide II band and BSA absorbance at 279 nm.

Spectral Analyses

Prior to spectral analysis, model compound and cartilage spectra were corrected for contributions from liquid water and residual atmospheric H_2O and CO_2 (supplemental Fig. S1).

Spectral Decomposition—We evaluated concentrations (c_j) of major extracellular matrix components by decomposing the spectra onto individual components. We used Beer's law, cartilage section thickness (h), and baseline-corrected integral intensities (A_i) of selected peaks in unpolarized spectra of the sample.

$$c_j = \sum_i \epsilon_{ji}^{-1} A_i / h \qquad \text{(Eq. 1)}$$

This decomposition accounted for overlap of peaks of individual components via the elements ϵ_{ji}^{-1} of the inverse of square matrix of absorptivities ϵ_{im} whose elements $\epsilon_{im} = A_{im}/(c_m l_m)$ are the integral intensities A_{im} of the ith peak of mth model compound normalized by the concentration of the compound c_m and path length l_m.

To increase accuracy, the peaks and their integration limits were selected so that the intensities A_{im} of a peak i were maximized for one compound and minimized for the others (Fig. 2 and supplemental Table S2).

A set of four peaks marked in Fig. 3*A* was used in the main text analysis. The other peaks were composed into independent sets and used for verification of the method.

Collagen Orientation—Collagen orientation was evaluated from dependence of IR absorption on the orientation of the absorbing chemical group with respect to IR light polarization. The dichroic difference spectra ($A_\parallel - A_\perp$) (Fig. 3*C*) recorded with IR light polarization parallel ($\parallel$) and perpendicular ($\perp$) to a selected direction were recorded and collagen orientation order parameters P and p were evaluated.

$$P = c_c < (2\cos^2\theta - 1)\cos^2\eta > \approx \frac{(A_\parallel - A_\perp)/l}{(A_\parallel - A_\perp)_0/(l_0 c_0)},$$

$$p = P/c_c \qquad \text{(Eq. 2)}$$

These parameters are related to angles between the collagen molecular axis and its projection onto the section plane, η, and between the projection and a selected direction in the plane, θ. Angle brackets $\langle \ldots \rangle$ denote averaging over the effective illuminated volume (~$6 \times 6 \times 12$ μm^3) determined by the actual spatial resolution and the sample thickness l; c_c is collagen concentration in this volume measured by the decomposition of depolarized spectra: $(A_\parallel + A_\perp)/2$. We used baseline-corrected integral intensity ($A_\parallel - A_\perp$) of the three bands in the amide III region (1135–1350 cm^{-1}) whose vibration dipoles are nearly parallel to the collagen helix axis (Fig. 3*B*). The $A_\parallel - A_\perp$ spectra are dominated by collagen because chemical groups of the other components have quasi-random orientations (Fig. 3*C*).

The sample intensity was normalized by the corresponding intensity $(A_\parallel - A_\perp)_0$ of a stretched, washed mouse tendon fiber and its collagen concentration c_0 and thickness l_0. The concen-

tration was determined from isotropic spectrum $(A_{\parallel} + 2A_{\perp})_0/3$. The fiber was a suitable model because it is composed of ~95% type I collagen whose spectra are similar to the spectra of collagen from all cartilage regions (Fig. 3*C* and supplemental Table S2).

Matrix Sampling, Definition of Cartilage Zones, and Statistical Analysis

Extracellular matrix areas (2–10 pixels) were selected based on visible images and HDIR hyperspectral images distinguishing matrix from cells (supplemental Fig. S4). The matrix areas were sampled in ~100-μm wide regions along the lines shown in Fig. 1 with a density of ~100 areas per mm^2. At the articular surface, 20–30 areas (2 × 2 pixels) were sampled on the inferomedial side every 8 μm. Accidentally damaged regions were excluded. HDIR and autoradiographic characteristics were averaged at selected positions of cartilage zones for each section.

The continuous epiphyseal cartilage of 0.5-day-old mice was divided into articular and growth plate regions based on their resemblance to articular cartilage and growth plate, which become separated by the secondary ossification center after 7–14 days. Each region was divided into zones defined morphologically (Fig. 1). The articular region was divided into the articular (*A*) zone, where cells were flattened, and the subarticular (*S*) zone, which began where most cells became round (about 140 μm below the articular surface). The boundary between the *S* and columnar (*C*) zones of the growth plate region was where most cells became flat and organized into stacks of two or more cells. The enlargement (*E*) zone began where the thickness (diameter along the bone axis) of most cells became 1.5 times larger than the thickness of the thinnest columnar cells. The hypertrophic (*H*) zone began where the thickness of most cells was ⅓ of the average thickness of cells where cell enlargement ceased and cartilage mineralization started. The mineralizing cartilage (*M*) zone began where septa of the mineralizing matrix appeared. The growth plate region ended at bone marrow where chondrocytes could no longer be distinguished. Within such definition, prehypertrophic zone is expected between the beginnings of the *E* and *H* zones. For data plotting, the growth plate zones of *dtd* were shifted so that the *H* zone beginning of *dtd* coincided with that of *wt*.

Mouse-to-mouse variability of the averaged spectroscopic and radiographic parameters at selected positions was analyzed by unequal variance, two-tail *t*-test. One section per mouse was included in the test because variation of the measured parameters between adjacent sections did not exceed the variation within a given region of a section.

HDIR Verification

Absence of several sampling, spectroscopic, and analytical artifacts was verified as detailed in supplemental Materials. In particular, we measured the matrix composition and its uncertainties using independent sets of spectral peaks, and compared the composition before and after enzymatic removal of GAG chains.

We found high correlation coefficients, $R^2 = 0.7–0.9$, and small deviations, ≤10%, between the independent measurements of the same compounds (supplemental Figs. S5 and S6).

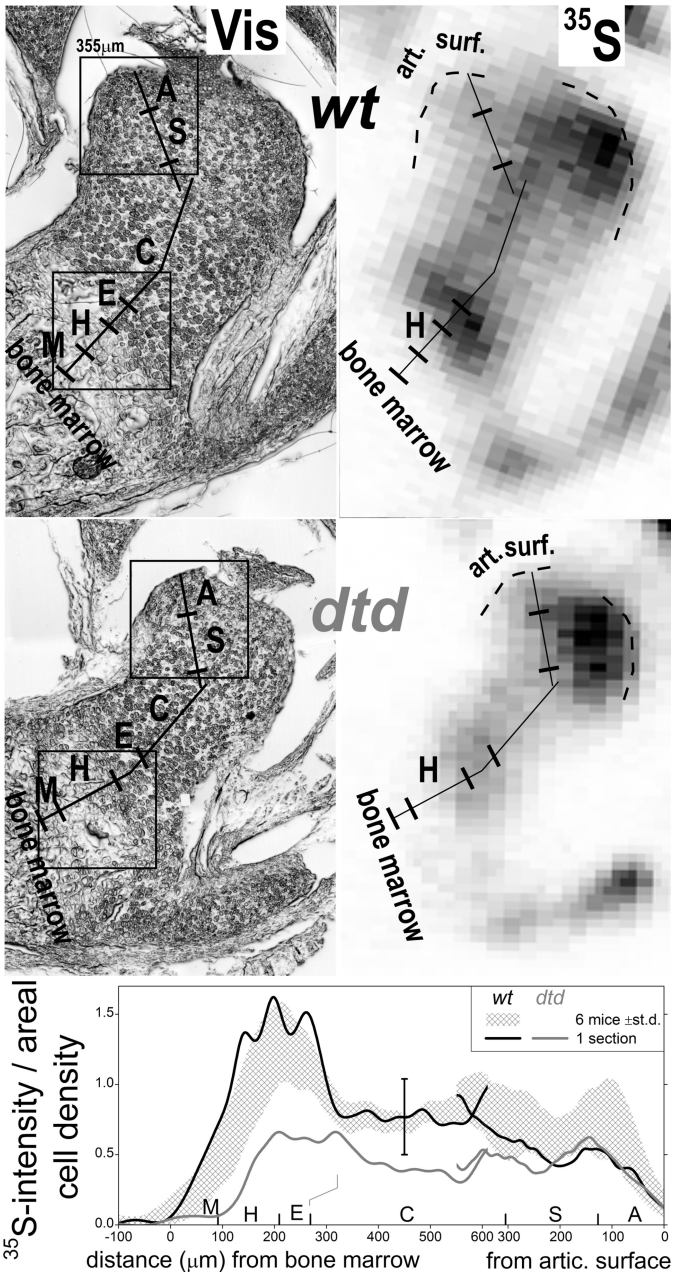

FIGURE 1. **Visible and ^{35}S-autoradiographic images of mid-coronal cryosections of proximal femur cartilage explants from 0.5-day-old *wt* and *dtd* mice.** *Left, Black lines* mark regions (within ~50 μm from the lines) where matrix composition and sulfate incorporation were sampled by HDIR imaging and autoradiography. *Squares* at the articular and growth plate regions illustrate some of the areas captured by HDIR. *Ticks* mark boundary between articular and subarticular zones and beginnings of columnar, enlargement, hypertrophic, mineralizing cartilage, and *bone marrow* zones defined morphologically under "Materials and Methods." *Right*, autoradiographic images of the sections that are shown on the *left* and contain [^{35}S]sulfate incorporated into the explants. The *black lines*, the zone ticks, and articular surface lines from the visible images were superimposed onto the ^{35}S images. Pixel darkness is proportional to the ^{35}S signal, with the darkness scale being the same for *wt* and *dtd*. *Bottom,* profiles of the ^{35}S-intensity divided by areal cell density along the *black lines* shown on *left images*. *Curves* are for single representative sections. The *hatched* band shows variability of profile shape for 3 *wt* and 3 normal, heterozygous littermates scaled to have the same average value in the middle of the columnar zone. The band is confined by mean ± S.D. curves. The *error bar* is S.D. of the unscaled intensity/density ratio at the middle of the columnar zone. The *zigzag line* marks shift of the *E* zone in *dtd* with respect to *wt*.

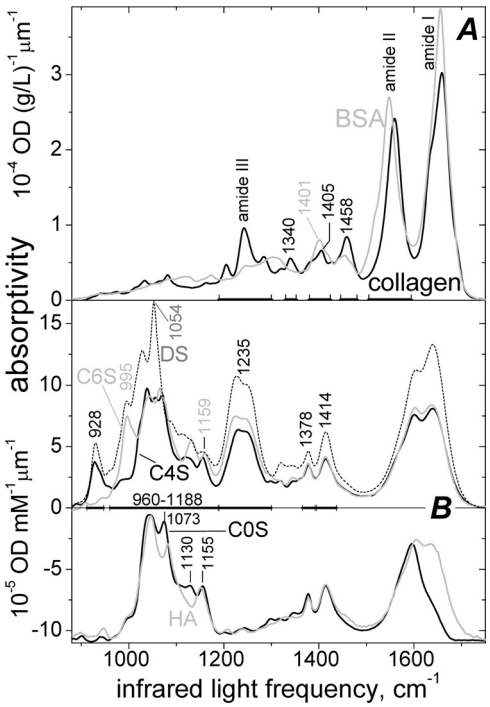

FIGURE 2. **HDIR absorption spectra of model compounds of cartilage extracellular matrix.** *A,* isotropic spectra of fibers reconstituted from purified bovine type II collagen and BSA modeling noncollagenous core proteins (*cf.* supplemental Figs. S2 and S3 and Table S2). *B,* spectra of chondroitins with C0S, C4S, and C6S forms of sulfation were derived by decomposition of spectra of highly enriched chondroitins. The available dermatan sulfate sample (*DS*) appeared contaminated by ~30% of GAGs other than HA or chondroitins (*cf.* supplemental Table S1). HA and C0S spectra were shifted down for clarity. *Bold horizontal segments* mark integration ranges of peaks used to analyze matrix composition.

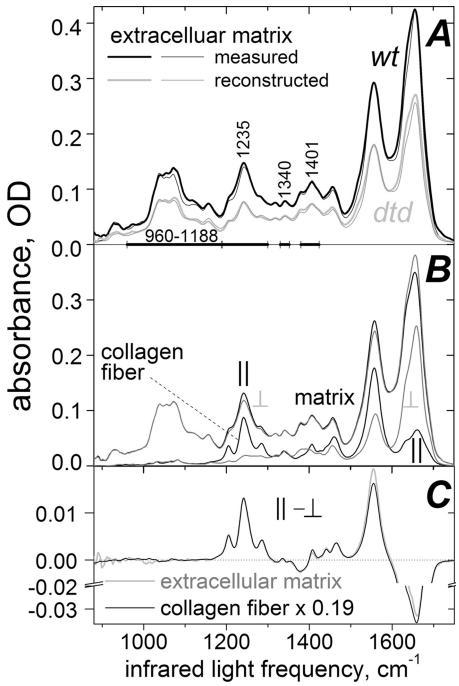

FIGURE 3. **HDIR absorption spectra of cartilage extracellular matrix and a collagen fiber.** *A,* matrix spectra from 5 × 5 μm^2 area 80 μm below the articular surface in *wt* and *dtd* mice are compared with spectra reconstructed from the model chondroitins, collagen type II, and BSA spectra based on decomposition of 4 spectral peaks marked by *horizontal segments*: collagen prolines 1340 cm^{-1} band, which is weak in NCPs due to low proline content; the CH_2 bending of NCP of the 1401 cm^{-1} band, which is shifted to 1405 cm^{-1} and is weaker in collagen due to the high glycine content; sugar ring bands between 960–1188 cm^{-1}, where the intensity of protein cores is weak; and GAG sulfate vibrations at 1235 cm^{-1}, where collagen also has a sizable contribution. *B,* polarized HDIR spectra of *wt* articular extracellular matrix and washed, stretched tendon fiber. The fiber spectra were normalized to have collagen content equivalent to that of the matrix. IR light polarization was parallel ∥ and perpendicular ⊥ to the articular surface or to the fiber axis. *C,* dichroic difference ∥ − ⊥ of the spectra shown in *B*. The fiber spectra at 1550–1700 cm^{-1} were distorted due to high absorbance.

Weak cross-correlation of different compounds, $R^2 = 0.04–0.2$, indicated that these compounds were resolved (supplemental Fig. S5). Reasonable quantification of the major matrix components was further suggested by reconstruction of matrix spectra from the model compounds spectra. The reconstruction based on decomposition of the main set of peaks reproduced the other peaks and fine structure of the peaks (Fig. 3*A*). We also estimated that interactions between major components within the matrix had a small effect on the spectra at our physiological-like conditions.

RESULTS

We examined sections of proximal femur cartilage of 0.5-day-old mice near anatomical lines shown in Fig. 1. We recorded infrared absorption spectra using a spectrometer attached to a microscope with a 128 × 128 array of detectors. Each recording collected spectra from a 355 × 355 μm^2 area with 2.8-μm nominal and 6–10-μm actual spatial resolution. The spectra exhibited peaks typical of extracellular matrix (Figs. 2, *A* and *B*, and 3*B*) or cells (not shown). Using these peaks, the matrix spectra were decomposed onto individual components dominating in cartilage matrix: GAGs, NCP, and collagen.

The resulting representative distributions of densities of each component in the articular and growth plate regions marked by *squares* in Fig. 1 are plotted as gray-scale images in Fig. 4. We also extracted data from small matrix areas near the anatomical lines (Figs. 1 and 4) and graphed them *versus* anatomical distances (Fig. 4). The graphed profiles were similar in every analyzed section of 6 *wt* and 6 *dtd* mice.

Such analysis showed that the components' distributions in *wt* and *dtd* mice were different. These differences were inferred from the main set of spectral peaks marked in Fig. 3*A*. Similar differences were derived from independent sets of other peaks shown in Figs. 2, *A* and *B*, and 3*B*, suggesting that the method's uncertainties were small (see supplemental Figs. S5 and S6 and Methods for HDIR verifications).

Glycosaminoglycans—The *dtd* mutant exhibited depletion of GAGs relative to *wt*, which occurred in the articular region only, 1.35–1.65 ± 0.35-fold, $p = 0.01–0.0001$, respectively, at 25–240 μm below the articular surface. (Mean ± S.E. for $n = 6$ *wt* and $n = 6$ *dtd* mice are reported, unless stated otherwise). The depletion normalized toward the columnar (*C*) zone of the growth plate region where it became insignificant, 1.1 ± 0.1-fold or less, $p = 0.2–0.7$ (see supplemental Methods and Fig. 1 for morphological definition of zones). Note that it is unclear if the decrease in densities of matrix components (Fig. 4, *A*, *C*, and *D*) in the hypertrophic (*H*) and mineralizing cartilage zones was real because thickness of the matrix septa became comparable

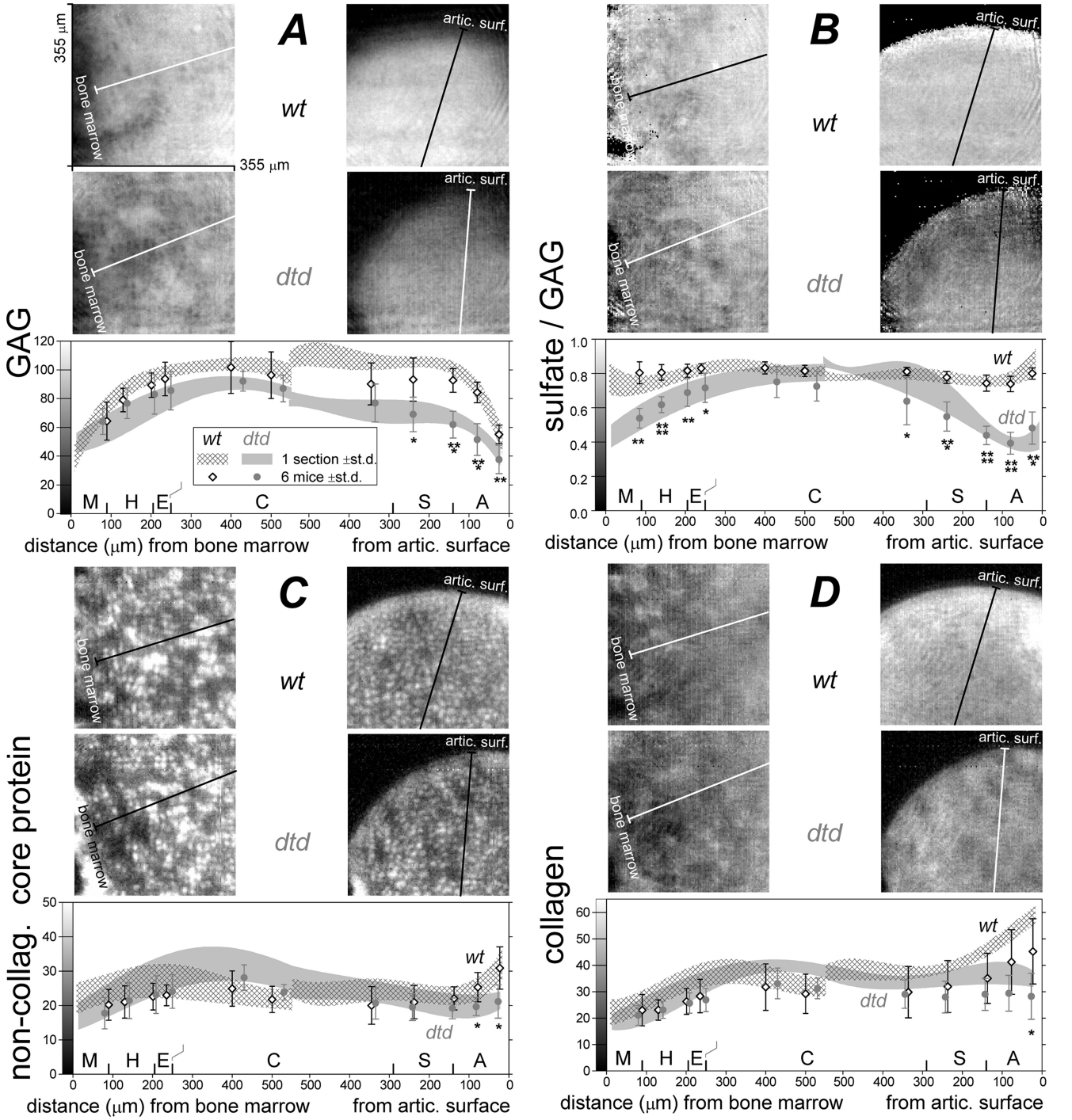

FIGURE 4. **Densities of GAGs, noncollagenous core proteins, and collagen and sulfate/GAG ratio in proximal femur cartilage of 0.5-day-old *wt* and *dtd* mice measured by HDIR hyperspectral imaging.** *Images*, hyperspectral images of articular and growth plate regions marked in Fig. 1. Pixel brightness is proportional to the densities and ratio according to vertical gray scale bars at *y* axes of graphs under the images. Pixels at cells appear darker in *D* or brighter in *C* than pixels at matrix due to, respectively, lower collagen or higher noncollagenous protein content at cells. The brightness of the cell pixels is quantitatively inaccurate. *Graphs,* the densities and ratio at the extracellular matrix areas near the anatomical lines (shown in *Images* and in Fig. 1) *versus* distance from the bone marrow and the articular surface. *Shaded* areas are confined by curves whose *y* values are mean ± S.D. at each distance for a single section (*cf.* supplemental Fig. S7). Points are mean ± S.D. for 6 mice at selected distances. *, **, ***, and **** denote *p* values ≤ 0.05, 0.005, 0.0005, and 0.00005, respectively. *Letters* and *ticks* mark the cartilage zones shown in Fig. 1. *Zigzag line* marks shift of the *E* zone in *dtd* with respect to *wt*. One unit of the *y* scales corresponds to: *A,* 1 ± 0.1 fmol/picoliter of chondroitins disaccharides or 0.5 ± 0.05 pg/picoliter of chondroitin sulfate disodium salt; *B,* 1 ± 0.07 sulfate/chondroitin disaccharide molar ratio; *C,* 1 ± 0.1 pg/picoliter of noncollagenous core proteins; *D,* 1 ± 0.1 pg/picoliter of triple helical collagens.

with the HDIR spatial resolution, resulting in marked "blurring" of HDIR images of the septa.

To confirm that GAG chains in 0.5-day-old mouse cartilage matrix were dominated by chondroitins, we exhaustively digested fixed *wt* and *dtd* sections in the HDIR chamber with testicular hyaluronidase, which cleaves and releases hyaluronate, chondroitin, and hybrid chondroitin/dermatan chains. The resulting intensity loss in IR absorption spectra (supplemental Fig. S6*B*) sug-

gested dominance of C4S and C0S. The estimated fraction of C6S was small (several percent), in agreement with a previous analysis of mice and rats (28) and HPLC analysis of whole 0.5-day-old femur heads, 3.1 ± 0.2% in *wt* and 3.3 ± 0.2% in *dtd*, $n = 4$ (calculated from our previous data (8)). Low intensity of the characteristic peaks of hyaluronate and dermatan indicated their small content (less than 10 and 5% of GAGs, respectively (supplemental Fig. S6, *A* and *B*)). This is consistent with previous biochemical analyses on neonatal mouse and bovine cartilages that can be summarized in GAG proportions of about 88% chondroitins, 7% hyaluronate, 0.4% dermatan, 5% keratan, and 1% heparan (9, 29–31).

Glycosaminoglycan Sulfation—Taking into account the dominance of chondroitins, we evaluated the sulfate/chondroitin disaccharide ratio (*cs*) in the matrix using the main set of peaks including bands of C4S and C6S sulfate groups at about 1235 cm^{-1} and sugar rings at 960–1188 cm^{-1} (Fig. 2*B*).

The apparent sulfation ratio *cs* varied across the proximal femur cartilage weakly in *wt*, but strongly in *dtd* (Fig. 4*B*). The strongest undersulfation occurred at the articular region 80 μm below the articular surface and at the *H* zone of *dtd*. The *dtd* sulfation was normalizing toward resting-like zone (expected before the columnar zone) and articular surface, and toward the columnar zone.

Specifically, *cs* was lowest at 80 μm below the articular surface and at *H* zone, $cs_{dtd}(80) = 0.39 \pm 0.03$ *versus* $cs_{wt}(80) = 0.74 \pm 0.02$, $p = 0.0002$, and $cs_{dtd}(H) = (0.54–0.69) \pm 0.03$ *versus* $cs_{wt}(H) = 0.81 \pm 0.02$, $p < 0.01$. At the columnar zone, *cs* became nearly normal, $cs_{dtd}(C) = 0.75 \pm 0.04$ *versus* $cs_{wt}(C) = 0.83 \pm 0.02$, $p = 0.08$, with the corresponding relative increase in ratio of *cs* being higher in *dtd* than in *wt*, $cs_{dtd}(C)/cs_{dtd}(80) = 1.64 \pm 0.14$ and $cs_{wt}(C)/cs_{wt}(80) = 1.1 \pm 0.02$, $p = 0.01$. At 25 μm below the articular surface, *cs* was also increased: ratio of *cs*'s at 25 and 80 μm, $cs_{dtd}(25)/cs_{dtd}(80) = 1.22 \pm 0.05$, was higher than in *wt*, $cs_{wt}(25)/cs_{wt}(80) = 1.08 \pm 0.02$, $p = 0.04$.

These results were consistent with independent measurements of sulfation by spectral decomposition involving the 928 cm^{-1} peak of C4S (supplemental Fig. S5), by analyzing the spectra of GAG chains released by hyaluronidase (supplemental Fig. S6*D*), and by HPLC disaccharide analysis of whole femur head, $cs_{dtd} = 68.2 \pm 0.8$ and $cs_{wt} = 90.4 \pm 0.3$, $n = 4$ (8). The *cs*'s determined by released chains spectra and HPLC were 5–10% higher than in Fig. 4*B* apparently due to small contributions from hyaluronate and oligosaccharides to the sugar ring bands used to measure *cs* in Fig. 4*B*. This error was smaller than the observed *dtd* defects and did not affect our conclusions.

The HDIR imaging (Fig. 4, *A* and *B*) was also consistent with reduced toluidine blue staining of sulfated GAGs in *dtd* (supplemental Fig. S8). The staining, however, could not distinguish between reduced GAG density and sulfation. In the articular region, the reduction was due to a decrease in both sulfation and GAG density. In the enlargement and hypertrophic zones, the staining remained intense despite undersulfation. Staining of human DTD samples at high and low pH values used to distinguish between unsulfated and sulfated GAGs did not allow unambiguous interpretation either (32).

Noncollagenous Core Proteins—Density of protein cores of all NCPs in the matrix of *dtd* was lower than that of *wt*, which

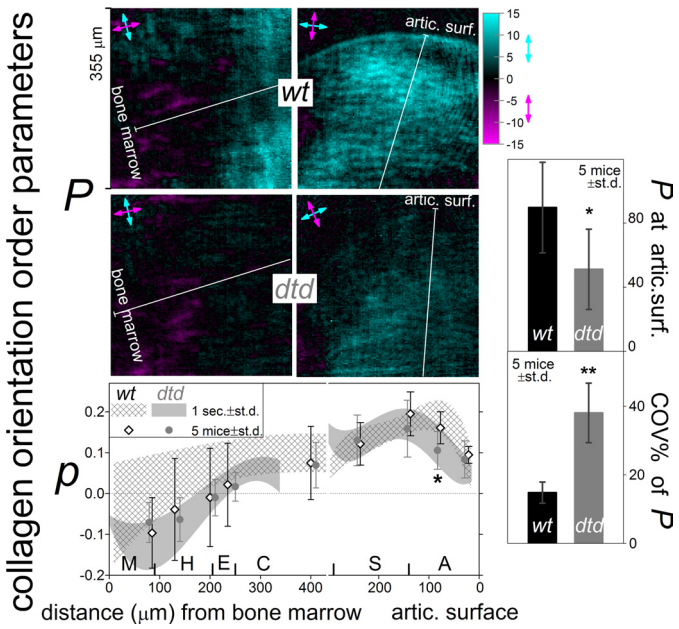

FIGURE 5. **Collagen orientation order parameters of matrix of proximal femur cartilage from 0.5-day-old *wt* and *dtd* mice measured by polarized HDIR hyperspectral imaging.** *Images,* parameter (*P*) uncorrected for collagen concentration. *Cyan* and *magenta* pixels mark areas with preferred collagen alignment indicated by *orthogonal arrows* of the corresponding color. The *cyan-black-magenta bar* corresponds pixel brightness to *P* values with 1 unit equal to 1 ± 0.1 pg/picoliter. *Bottom,* parameter (*p*) corrected for collagen concentration sampled at extracellular matrix near the lines (shown in these images and in Fig. 1) *versus* distance from the bone marrow and articular surface. *Shaded areas* represent mean ± S.D. for a single section (*cf.* supplemental Fig. S7*E*). *Letters* and *ticks* mark the cartilage zones shown in Fig. 1. *Right*, parameter (*P*) and its coefficient of variation *CV* at the articular surface. * and ** denote *p* values ≤ 0.05 and 0.005, respectively.

occurred at the articular region only (Fig. 4*C*): *wt*/*dtd* density ratio was 1.5 ± 0.2, $p = 0.01$, and 1.3 ± 0.1, $p = 0.02$, at 25 and 80 μm below the articular surface, respectively, and (0.9–1.1) ± 0.1, $p = 0.2–0.9$, at deeper articular layers and the growth plate region.

Collagen Content—Likewise, density of all triple helical collagens in the matrix of *dtd* was lower than that of *wt* at the articular region only (Fig. 4*D*): the *wt*/*dtd* ratio was 1.6 ± 0.3, $p = 0.02$, and 1.4 ± 0.2, $p = 0.07$, at 25 and 80 μm below the articular surface, respectively, and (0.9–1.1) ± 0.15, $p = 0.2–0.9$, at deeper articular regions and at the growth plate region.

Collagen Orientation—We quantified collagen orientation across the sections using HDIR hyperspectral imaging with IR light polarized in two orthogonal directions with respect to the articular surface and the growth plate plane. A resulting collagen orientation order parameter *P* (Equation 2) is plotted as images with two colors marking areas where collagen is preferentially oriented parallel or perpendicular to the selected directions (Fig. 5).

The images in Fig. 5 indicate that the amount of preferentially aligned collagen varies across different cartilage regions. As collagen density also varied (Fig. 4*D*), we plotted order parameter $p = P/c_c$ normalized for the collagen density c_c for 15–50 μm^2 areas of matrix (*lower left panel* of Fig. 5). In *wt*, this parameter varied between $|p| = 0.0$ and 0.25. This range would correspond to 0–25% of oriented molecules in a system where a fraction $(1 - |p|)$ of molecules is randomly oriented and the

other fraction $|p|$ is aligned ideally in the section plane and at zero angle to a preferred direction (33). Because aligned molecules have nonideal distribution of alignment angles, the actual oriented fraction is larger than 0–25%.

In *dtd*, distribution of collagen orientation was qualitatively similar, but absolute values of the orientation order parameters were reduced in the articular region (Fig. 5). The strongest reduction was ~80 μm below the articular surface, $p_{wt}/p_{dtd} = 1.5 \pm 0.3$, $p = 0.046$ (5 *wt* and 5 *dtd* mice). It normalized toward deeper and shallower regions, $p_{wt}/p_{dtd} = (1.1–1.25) \pm (0.2–0.3)$, $p = 0.2–0.6$, with the collagen disorientation parameter, p_{wt}-p_{dtd}, being higher at the 80 μm depth than at 25 and 240 μm, $p = 0.05$ and $p = 0.001$, respectively.

Substantial disorientation also occurred in the thin layer of collagen at the articular surface where the order parameter P was $P_{wt}/P_{dtd} = 1.8 \pm 0.3$ times lower in *dtd* ($p = 0.05$, Fig. 5). Furthermore, the layer was diffuse in *dtd*, but sharp and thin in *wt* in every analyzed section (Fig. 5). Because the layer thickness in *wt*, ~5 μm, was comparable with the HDIR spatial resolution, ~6 μm, the measured P_{wt} values were underestimated (the image of the layer in Fig. 5 was blurred). Thus, the actual P_{wt}/P_{dtd} ratio should be even higher.

In addition, the surface collagen layer in *dtd* was highly heterogeneous along the articular surface: coefficient of variation (CV = S.D./mean) of its parameter P was higher than in *wt* ($CV_{dtd}/CV_{wt} = 2.6 \pm 0.4$, $p = 0.002$). The *dtd* variation was so high, $CV_{dtd} = 0.38 \pm 0.04$, that the p values were two or more times lower than average at ~10% of the surface in *dtd*. The corresponding surface fraction would be ~0.04% in *wt* (assuming normal distribution), but such poorly organized areas were not found in any *wt* section.

At the growth plate regions, the order parameters had high sample-to-sample variability which obscured differences between *wt* and *dtd*, if any (Fig. 5).

Chondroitin Synthesis Rate—To relate GAG composition and synthesis, we analyzed [^{35}S]sulfate incorporation into femur explants incubated shortly after excision from 0.5-day-old mice. In the resulting autoradiographs of explants cryosections, intensity distribution was similar for 4- (Fig. 1) and 2-h (not shown) incubations, suggesting that these profiles were not limited by [^{35}S]sulfate diffusion (as expected from ~20 min diffusion time estimated from sulfate diffusion coefficient in cartilage (34) and the explant geometry). Because ~90% of sulfate groups of this mouse cartilage belongs to chondroitin sulfate, and, because ~5% variability of chondroitin sulfation levels in *wt* was smaller than severalfold variability of incorporation levels, the radiographs reflected variability of chondroitin synthesis rates in *wt*.

From the [^{35}S]sulfate incorporation images, we extracted profiles for the same regions sampled in the HDIR experiment (Fig. 1). The ^{35}S intensities were normalized by areal cell density to correct for its ~10-fold variability. We pooled together 3 *wt* and 3 heterozygous littermates because *wt* and heterozygous mice had indistinguishable radiographic profiles (supplemental Fig. S9*C*), chondroitin sulfation, sulfate uptake, and morphologic and phenotypic characteristics (8). The resulting profile and its variability were plotted in Fig. 1 (*bottom*). The pooled data were also plotted in Fig. 6 after correcting for the fact that the areal cell density underestimates volumetric density of smaller cells. We verified that data processing uncertainties, ~15%, were smaller than the following observed effects.

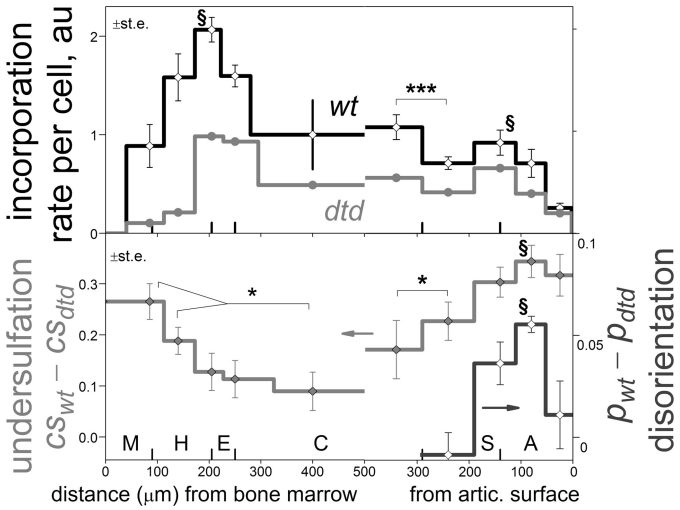

FIGURE 6. **Correlation between chondroitin synthesis rate per cell, chondroitin undersulfation in *dtd*, and collagen disorientation in *dtd* at selected distances.** *Top*, [^{35}S]sulfate incorporation rate per cell for 6 normal (3 *wt* and 3 heterozygous, denoted *wt*) and 1 *dtd* littermates. For normal mice, the rate profiles were scaled to have the same average value at the middle of the columnar (*C*) zone. The *vertical bar* at the *C* zone is standard error of the unscaled rate. *Bars* at the other positions are S.E. of the scaled values. The incorporation rate reflects the chondroitin synthesis rate per cell in *wt*, but underestimates the synthesis rate in *dtd*. *Bottom*, differences between *wt* and *dtd* for chondroitin sulfation ratio *cs* and collagen orientation order parameter *p* replotted from Figs. 4*B* and 5. In our definition, the chondroitin undersulfation and collagen disorientation decrease with cs_{dtd} and p_{dtd} getting closer to cs_{wt} and p_{wt}. *Error bars* are S.E. of the *cs* and *p* differences. All data were measured at similar anatomical positions and plotted at the positions of a *wt* sample. * denotes *p* values ≤ 0.05. § indicates statistically significant (*p* values ≤ 0.05) peaks.

The proximal femur cartilage showed two peaks in the incorporation profiles: near the boundary between articular and subarticular zones and near the beginning of the *H* zone (Figs. 1 and 6). Specifically, the incorporation rate per cell at the subarticular peak was 3.8 ± 0.3 and 1.27 ± 0.06 times higher than at shallower (25 μm) and deeper (240 μm) distances from the articular surface, respectively ($p = 0.0004$ and $p = 0.008$, one-sample, two-tail *t*-test). The rate at the *H* zone peak was 2.1 ± 0.1 and 4.3 ± 1.7 higher than at the middle of the columnar and beginning of mineralizing cartilage zones, $p = 0.0004$ and $p = 0.05$, respectively.

In a *dtd* mouse, the incorporation profiles in proximal and distal femoral cartilages had shapes similar to its *wt* littermates (Figs. 1, 6, supplemental Fig. S10). The incorporation intensities in *dtd* were 1.5–2 times lower than in *wt*. The corresponding difference in chondroitin synthesis rate should be smaller because the sulfate/chondroitin ratio in *dtd* is 1.1–1.9 lower than in *wt* and because a non-negligible fraction of incorporated sulfate in *dtd* originates from intracellular catabolism of sulfur-containing compounds (35, 36). The semi-quantitative similarity of the incorporation profiles indicates that uptake of extracellular sulfate was still the major source of intracellular sulfate in *dtd*. The similarity also indicates that the chondroitin synthesis rates in *wt* and *dtd* had similar profiles and absolute values differing less than 2-fold.

Although we had only one *dtd* mouse in the two litters used for radiolabeling, its phenotype and cartilage morphology were typical of all *dtd* mice. Because the sulfate incorporation measurement underestimates the chondroitin synthesis rate in *dtd*, it was not pursued further.

Note that similar incorporation profiles were observed in other epiphyseal cartilages. We found that the distal femurs had a wider peak at the *H* zone due to wider distal zones (supplemental Fig. S10). Qualitatively similar profiles were found for distal tibia explants from chick embryos and for *in vivo* incorporation into humeri of 4- and 7-day-old rats (37–40). It has been unclear, however, if those profiles were distorted by limited [^{35}S]sulfate diffusion during very short (5 min) incubation of the explants and by variable cell density or by terminal cell hypertrophy initiating secondary ossification center in the articular region of rat humeri at 7 days.

Correlation between Chondroitin Synthesis and Matrix Disruptions—The radiographic and sulfation profiles are plotted together in Fig. 6. This plot indicates that undersulfation of chondroitin correlated with its synthesis rate in the articular region of *dtd*. Such correlation seems to hold also in the growth plate region, although undersulfation increased through this region while the rate increased and then declined. Because cells and their matrix progress from columnar to the mineralizing zone, progression in matrix composition reflects accumulation of chondroitin chains made through these zones rather than composition of chains made at each location. Synthesis in the middle of the *H* zone of chains whose sulfation is higher than that of chains made in the beginning of the *H* zone but lower than in the columnar zone can explain the observed decrease in the net sulfation across the *H* zone.

Disorientation of collagen in the articular region of *dtd* also correlated with the chondroitin synthesis rate and chondroitin undersulfation (Fig. 6). In the growth plate region, high variability of the measured orientation parameters obscured such correlation, if any.

DISCUSSION

In chondrocytes, the SLC26A2 sulfate/chloride antiporter is the main source of inorganic sulfate. Most of this sulfate is spent to sulfate chondroitin, which is then secreted to constitute ~90% of cartilage extracellular GAGs. The homozygous A386V mutation knocked into the antiporter reduces the sulfate transport rate into chondrocytes from *dtd* mouse (8). This reduction causes chondroitin undersulfation and yet a barely detectable clinical phenotype at birth (8).

Undersulfation Varies Across Cartilage and Correlates with Chondroitin Synthesis Rate—We found that the undersulfation was mild in most regions of epiphyseal cartilage, but strong in (sub)articular and (pre)hypertrophic zones of the growth plate region (Fig. 4*B*). The undersulfated regions gave small contributions to the net sulfation of the whole tissue because they were narrow and had thin matrix and lower GAG content (Fig. 4*A*, and supplemental Figs. S4 and S8). Yet, these regions are crucial for cartilage and bone development and maintenance, suggesting that the undersulfation variability may be a clue to DTD bone malformation and joint degradation.

In growing cartilage of newborn mice, matrix composition should be dominated by matrix synthesis rather than degradation. The rate of chondroitin synthesis in cartilage explants was also highly variable across the epiphyseal cartilage in both *wt* and *dtd* (Fig. 1). Furthermore, the synthesis rate and the undersulfation of chondroitin correlated (Fig. 6).

Variation of Matrix Synthesis Rate Is Related to Cartilage Growth—Profile of the chondroitin synthesis rate showed two peaks (Fig. 1), which seem related to cell/matrix morphology of the growing cartilage. In the upper (proximal to the articular surface) part of the columnar zone, the stacked cells are thin and their proliferation is accompanied by production of a thin layer of matrix. In the lower part of the growth plate, the cells stop proliferating, but enlarge their size and augment their matrix volume per cell up to 2.7 times by the end of the hypertrophy (despite making matrix septa thinner) (41). Because density of GAGs, collagen, and NCPs within the matrix changes little between columnar and hypertrophic zones, the matrix augmentation requires synthesis of matrix components such as chondroitin (Fig. 1). At the end of cell enlargement, matrix augmentation and synthesis slow down, resulting in the peak in the profile of chondroitin synthesis rate (Fig. 1). We expect the main carrier of chondroitin chains aggrecan and perhaps other components to follow a similar synthesis rate profile, as observed for collagen in chick embryo explants (37).

Cartilage matrix provides mechanical integrity to growth plate that must withstand mechanical loads in growing bone. About 75% of the axial bone growth occurs at the chondrocyte enlargement zone (41, 42). Therefore, the elevated matrix synthesis in enlarging chondrocytes is needed, at least, to support bone integrity during growth.

Whether the elevated chondroitin synthesis is also a driving force for chondrocyte enlargement is unclear. Of three forces hypothesized so far, static hydration pressure of chondroitin sulfate proteoglycans (which swell matrix around chondrocytes) does not seem dominating: chondroitin sulfate density and, hence, hydration pressure at the columnar zone are similar to those at the enlargement and hypertrophic zones (Fig. 4*B*) but the columnar chondrocytes do not enlarge. However, we cannot completely exclude a second force due to dynamic hydration pressure from sulfated proteoglycans secreted and transiently concentrated near cells because our measurements cannot resolve pericellular matrix. If this force contributes, the nearly 2-fold reduction in chondroitin sulfation, believed to be the main cause of the pressure, is insufficient to appreciably reduce enlargement in the *dtd* growth plate region.

The third hypothesized force driving cell enlargement is exerted from within chondrocytes by synthesizing intracellular components and uptaking water (43). This force does not seem to have substantial contribution from the elevated chondrotin sulfate synthesis because sulfation occurs in Golgi whose volume is small and does not augment (43). However, elevated synthesis of matrix proteins may contribute indirectly because it is accompanied by ~2.5-fold volumetric augmentation of the synthetic apparatus, endoplasmic reticulum, whose volume fraction per cell is substantial, ~15% (43).

Profile of chondroitin synthesis rate across the articular cartilage also seems related to growing morphology. In the articu-

lar zone up to ~80 μm below the articular surface, chondrocytes are small and need to synthesize little chondroitin sulfate because its density within the matrix is low and the matrix is thin (Fig. 4*B*, and supplemental Figs. S4 and S8). In the subarticular zone, cells enlarge, proliferate, and augment their matrix volume and GAG density in the matrix (Fig. 4*B* and supplemental Figs. S4 and S8), which requires elevated rates of matrix synthesis. The synthesis rate drops toward a subzone preceding the columnar zone. This subzone often called "resting" does not show a dramatic increase in matrix thickness, GAG density, and cell size, resulting in a lower synthesis rate and in a peak in the rate profile. Thus, such chondrocyte enlargement concomitant with elevated chondrotin synthesis at the subarticular zone may contribute to growth of articular cartilage as well.

Rapid Chondroitin Synthesis Creates Sulfate Deficit—The chondroitin sulfation inversely correlated with the chondroitin synthesis rate in *dtd* but not in *wt* (Fig. 6). We interpret such dependences via balance of sulfate supply, sulfate consumption by chondrotin sulfate synthesis/secretion, and enzymatic activity of intermediate steps of the sulfation pathway. The activity determines a threshold below which sulfation efficiency becomes dependent on its substrate, intracellular inorganic sulfate. In *wt*, the efficiency (sulfate/chondroitin ratio, *cs*) remains close to 100% and the sulfate remains above the threshold at any physiological rates of sulfate consumption.

In *dtd*, the reduced sulfation indicates that the intracellular sulfate reaches the threshold. The undersulfation would be trivially determined by the law of mass conservation, $cs \leq V_S/V_C$, if the chondrotin synthesis rate V_C is much faster than rate of intracellular sulfate generation V_S. This would happen when chondroitin is strongly undersulfated, $cs \ll 1$. When the undersulfation is mild, as in *dtd* and nonlethal patients, it can depend on the enzymatic activity as well.

The *in vivo* correlation suggests that the chondrotin synthesis rate is the primary factor determining the intracellular sulfate deficit and the undersulfation in *dtd* cartilage. Activity of other steps of the sulfation and sulfate production pathway seems to have secondary, yet non-negligible compensating effects on the undersulfation. This is indicated by breakdown of the correlation upon transition from growth plate to articular region (Fig. 6): The columnar zone had a higher synthesis rate, but better sulfation than the resting-like and peri-articular subzones.

The undersulfation-synthesis rate correlation can explain the normalizing sulfation in *dtd* mice with age (8). As growth and chondroitin synthesis slow down with age (44), sulfation of newly synthesized chains should increase. The correlation, however, does not explain rapid progression of skeletal deformities and articular cartilage degradation with age despite the normalizing sulfation (8).

Reduced Collagen Orientation May Cause Cartilage Degradation—We found other matrix abnormalities potentially related to the articular degradation. First, densities of the major components, GAGs, collagen, and NCP, were reduced at the articular region *only*, indicating pathological processes specific to this region (Fig. 4, *A*, *C*, and *D*).

Second, collagen was partly disorientated in the articular region in *dtd* (Fig. 5), which could contribute to the proteoglycan depletion and the degradation (Fig. 4). The disorientation affected a thin layer of well oriented, densely packed collagen fibers normally present at the articular surface. This layer protects the articular cartilage from frictional damage by articulation of the opposite bone and, perhaps, from degrading enzymes whose concentration in synovial fluid may be higher than in cartilage. Its malformation may also lead to diffusional loss of proteoglycans and growth factors from the articular region and penetration of extraneous factors from synovial fluid, compromising functions of the whole joint.

Origin of Collagen Disorientation—Disruption of the surface layer occurs at early stages of joint degeneration in another genetic pathology (45) and in arthritis. Despite different causes, arthritic and DTD humans and mice exhibit common signs of chondrocyte and matrix degeneration including proteoglycan depletion from the articular region and accumulation of thick collagen fibrils (32, 46–50), indicating potentially common intermediate mechanisms of degradation. In degenerating arthritic and DTD cartilages, accumulating collagen fibers often appear irregularly oriented (32, 46–50), which should reduce collagen orientation order parameters. The lack of accumulation-disorientation correlation (Figs. 4*D* and 5) suggests that the accumulation is not the primary cause of the disorientation in *dtd*.

Collagen disorientation correlated with undersulfation and, likely, with the inorganic sulfate deficit (Fig. 5), indicating that sulfated species may be involved in processes of collagen orientation in growing articular cartilage in *dtd*. Because the disorientation appears in *dtd* cartilage whose sulfation and organization are perturbed by impaired sulfate transport mildly, the same sulfation-dependent processes may be involved in collagen orientation in *wt* cartilage as well.

Which Undersulfated Species Cause DTD?—Although this and previous works indicate a relationship of cartilage dysfunctions to chondroitin undersulfation, it is unclear if undersulfation of chondroitin is the direct cause of DTD. Chondrocytes of *dtd* and other mice with sulfation pathway defects accompanied by chondroitin undersulfation show reduced Indian Hedgehog (IHH) signaling and reduced proliferation (seen in the growth plate region (51–53), in the *dtd* articular region (supplemental Fig. S8) and in *dtd* cell culture (8)). Proliferation in cartilage is partly regulated by long range IHH and parathyroid hormone-related protein signalings generated by the prehypertrophic and articular zones (54, 55), which experience the strongest undersulfation in *dtd*. In *brachimorphic* mouse with impaired synthesis of the organic sulfate donor, the IHH reduction has been ascribed to IHH binding to C4S whose content is reduced 1.3-fold (51). However, in a mouse chondrodysplasia caused by C4S-sulfotransferase knock-out with 20-fold C4S reduction, IHH signaling is unaffected, but dysfunctions have been ascribed to other factors (9).

Apart from chondroitin, other sulfated species are present in cartilage in minor amounts, but known to affect signaling and matrix. For example, cholesterol sulfate regulates the synthesis pathway of cholesterol (56–58), a key regulator of IHH signaling at the protein level. Also, heparan sulfate is a co-factor of several signaling receptors and growth factors (59–61); heparan sulfate undersulfation has been hypothesized to disorganize

collagen (62) because suppression of sulfation or synthesis of a heparan sulfate proteoglycan in a cancer cell line or zebrafish embryos disorganizes fibronectin (62, 63). A connection between undersulfation of minor species and of chondroitin has been hypothesized because all species accept the sulfonate group from 3′-phosphoadenosine 5′-phosphosulfate (PAPS) synthesized from inorganic sulfate. Whether this connection is significant depends on multiple enzymatic and transport steps whose kinetic relationships *in vivo* are not understood.

The observed dependence of undersulfation of chondroitin on its synthesis rate indicates that the PAPS concentration in *dtd* drops to the Michaelis constant for PAPS of chondroitin-4-sulfotransferase, K_m ~0.3 μM (64). Such concentration is lower than the K_m of sulfotransferases to heparan, 0.4–100 μM, and cholesterol, 2–7 μM (65–69). Therefore, such species may be undersulfated, and the domain structure of heparan sulfate implicated in signaling may be disrupted (70) in the regions with substantial chondroitin undersulfation. As these regions are narrow, undersulfation of minor species may be difficult to detect by existing analyses requiring samples larger than a mouse limb. Analytical advances and manipulation of genes may further clarify mechanisms of DTD and its high phenotype variability even between siblings (13).

Implications for Cartilage Growth—At present, we obtained evidence that sulfate deficit causes disorientation of cartilage collagen in the studied mouse background, suggesting that processes involved in collagen orientation may depend on sulfated species.

We observed that the chondroitin synthesis rate per cell varies ~10-fold across growing epiphyseal cartilage and peaks at the subarticular and pre-hypertrophic regions. The latter peak supports matrix and cell enlargement near the pre-hypertrophic zone and, therefore, may be needed for robust bone growth driven by the enlargement.

Implications for Chondrodysplasias—We observed correlations of undersulfation and collagen disorientation with chondroitin synthesis rate across cartilage with mildly impaired sulfation.

This example suggests that rapid matrix synthesis in pre-hypertrophic and subarticular regions can make these narrow, yet vital regions particularly susceptible to mutations whose adverse effects increase with the synthesis rate of matrix molecules. This may apply, for example, to chondrodysplasias whose mutations in aggrecan or other matrix molecules can cause endoplasmic reticulum stress. The stress and the resulting defects increase with the number of mutant alleles and, hence, with the synthesis rate (71–73).

For DTD, the observed correlations imply that improving sulfation during development may improve formation of bone, articular cartilage, and the periarticular collagen layer and thereby reduce predisposition to joint degradation at older age when the rate diminishes. These correlations may help to determine the kinetic regime of the *in vivo* sulfation pathway, develop its theoretical model, and predict pathway steps that can be targeted for improving sulfation. Targeting treatments are difficult to deliver to deep avascular cartilage regions. Observed in this work proximity of the most affected regions to synovial fluid and bone marrow provides a hope for systemic delivery from blood circulation.

Acknowledgments—We thank Dr. E. Makareeva for help in SDS-PAGE analysis of collagen composition and V. Krevinko in cell counting.

REFERENCES

1. Hästbacka, J., de la Chapelle, A., Mahtani, M. M., Clines, G., Reeve-Daly, M. P., Daly, M., Hamilton, B. A., Kusumi, K., Trivedi, B., and Weaver, A. (1994) The diastrophic dysplasia gene encodes a novel sulfate transporter. Positional cloning by fine-structure linkage disequilibrium mapping. *Cell* **78,** 1073–1087
2. Faiyaz ul Haque, M., King, L. M., Krakow, D., Cantor, R. M., Rusiniak, M. E., Swank, R. T., Superti-Furga, A., Haque, S., Abbas, H., Ahmad, W., Ahmad, M., and Cohn, D. H. (1998) Mutations in orthologous genes in human spondyloepimetaphyseal dysplasia and the brachymorphic mouse. *Nat. Genet.* **20,** 157–162
3. Thiele, H., Sakano, M., Kitagawa, H., Sugahara, K., Rajab, A., Höhne, W., Ritter, H., Leschik, G., Nürnberg, P., and Mundlos, S. (2004) Loss of chondroitin 6-*O*-sulfotransferase-1 function results in severe human chondrodysplasia with progressive spinal involvement. *Proc. Natl. Acad. Sci. U.S.A.* **101,** 10155–10160
4. Hermanns, P., Unger, S., Rossi, A., Perez-Aytes, A., Cortina, H., Bonafé, L., Boccone, L., Setzu, V., Dutoit, M., Sangiorgi, L., Pecora, F., Reicherter, K., Nishimura, G., Spranger, J., Zabel, B., and Superti-Furga, A. (2008) Congenital joint dislocations caused by carbohydrate sulfotransferase 3 deficiency in recessive Larsen syndrome and humero-spinal dysostosis. *Am. J. Hum. Genet.* **82,** 1368–1374
5. Orkin, R. W., Williams, B. R., Cranley, R. E., Poppke, D. C., and Brown, K. S. (1977) Defects in the cartilaginous growth plates of brachymorphic mice. *J. Cell Biol.* **73,** 287–299
6. Schwartz, N. B., Lyle, S., Ozeran, J. D., Li, H., Deyrup, A., Ng, K., and Westley, J. (1998) Sulfate activation and transport in mammals. System components and mechanisms. *Chem. Biol. Interact.* **109,** 143–151
7. Bullock, S. L., Fletcher, J. M., Beddington, R. S., and Wilson, V. A. (1998) Renal agenesis in mice homozygous for a gene trap mutation in the gene encoding heparan sulfate 2-sulfotransferase. *Genes Dev.* **12,** 1894–1906
8. Forlino, A., Piazza, R., Tiveron, C., Della Torre, S., Tatangelo, L., Bonafè, L., Gualeni, B., Romano, A., Pecora, F., Superti-Furga, A., Cetta, G., and Rossi, A. (2005) A diastrophic dysplasia sulfate transporter (SLC26A2) mutant mouse. Morphological and biochemical characterization of the resulting chondrodysplasia phenotype. *Hum. Mol. Genet.* **14,** 859–871
9. Klüppel, M., Wight, T. N., Chan, C., Hinek, A., and Wrana, J. L. (2005) Maintenance of chondroitin sulfation balance by chondroitin-4-sulfotransferase 1 is required for chondrocyte development and growth factor signaling during cartilage morphogenesis. *Development* **132,** 3989–4003
10. Frederick, J. P., Tafari, A. T., Wu, S. M., Megosh, L. C., Chiou, S. T., Irving, R. P., and York, J. D. (2008) A role for a lithium-inhibited Golgi nucleotidase in skeletal development and sulfation. *Proc. Natl. Acad. Sci. U.S.A.* **105,** 11605–11612
11. Walker, B. A., Scott, C. I., Hall, J. G., Murdoch, J. L., and McKusick, V. A. (1972) Diastrophic dwarfism. *Medicine* **51,** 41–59
12. Horton, W. A., Rimoin, D. L., Lachman, R. S., Skovby, F., Hollister, D. W., Spranger, J., Scott, C. I., and Hall, J. G. (1978) The phenotypic variability of diastrophic dysplasia. *J. Pediatr.* **93,** 609–613
13. Mäkitie, O., and Kaitila, I. (1997) Growth in diastrophic dysplasia. *J. Pediatr.* **130,** 641–646
14. Rossi, A., Kaitila, I., Wilcox, W. R., Rimoin, D. L., Steinmann, B., Cetta, G., and Superti-Furga, A. (1998) Proteoglycan sulfation in cartilage and cell cultures from patients with sulfate transporter chondrodysplasias. Relationship to clinical severity and indications on the role of intracellular sulfate production. *Matrix Biol.* **17,** 361–369
15. Lamb, R., Thomson, W., British Society of Paediatric and Adolescent Rheumatology, Ogilvie, E. M., and Donn, R. (2007) Positive association of SLC26A2 gene polymorphisms with susceptibility to systemic-onset juve-

nile idiopathic arthritis. *Arthritis Rheum.* **56,** 1286–1291
16. Forlino, A., Gualeni, B., Pecora, F., Torre, S. D., Piazza, R., Tiveron, C., Tatangelo, L., Superti-Furga, A., Cetta, G., and Rossi, A. (2006) Insights from a transgenic mouse model on the role of SLC26A2 in health and disease. *Novartis Found. Symp.* **273,** 193–206; discussion 206–212, 261–264
17. Gualeni, B., Rossi, A., Geoffrey, V., Marty-Morieux, C., Forlino, A., Pecora, F., Houillier, P., and de Vernejoul, M. (2007) Morphological and biochemical characterization of bone phenotype in a chondrodysplasia mouse model. *Calcif. Tissue Int.* **80,** S77-S78
18. Superti-Furga, A. (2002) in *Connective Tissue and Its Heritable Disorders* (Royce, P. M., and Steinmann, B., eds) 2nd Ed., pp. 939–960, Wiley-Liss, New York
19. Potter, K., Kidder, L. H., Levin, I. W., Lewis, E. N., and Spencer, R. G. (2001) Imaging of collagen and proteoglycan in cartilage sections using Fourier transform infrared spectral imaging. *Arthritis Rheum.* **44,** 846–855
20. Camacho, N. P., West, P., Torzilli, P. A., and Mendelsohn, R. (2001) FTIR microscopic imaging of collagen and proteoglycan in bovine cartilage. *Biopolymers* **62,** 1–8
21. Boskey, A., and Pleshko Camacho, N. (2007) FT-IR imaging of native and tissue-engineered bone and cartilage. *Biomaterials* **28,** 2465–2478
22. Rieppo, J., Hyttinen, M. M., Halmesmaki, E., Ruotsalainen, H., Vasara, A., Kiviranta, I., Jurvelin, J. S., and Helminen, H. J. (2009) Changes in spatial collagen content and collagen network architecture in porcine articular cartilage during growth and maturation. *Osteoarthritis Cartilage* **17,** 448–455
23. Yin, J., and Xia, Y. (2010) Macromolecular concentrations in bovine nasal cartilage by Fourier transform infrared imaging and principal component regression. *Appl. Spectrosc.* **64,** 1199–1208
24. Dukor, R. K. (2002) in *Applications of Vibrational Spectroscopy in Life, Pharmaceutical and Natural Sciences* (Chalmers, J. M., and Griffiths, P. R., eds) pp. 3335–3361, John Wiley & Sons, New York
25. Mertz, E. L., and Sullivan, J. V. (2008) Flow-through, thermal expansion-compensated cell for light spectroscopy. United States patent 7,355,697
26. Mertz, E. L., and Leikin, S. (2004) Interactions of inorganic phosphate and sulfate anions with collagen. *Biochemistry* **43,** 14901–14912
27. Torchia, D. A., Hasson, M. A., and Hascall, V. C. (1977) Investigation of molecular motion of proteoglycans in cartilage by ^{13}C magnetic resonance. *J. Biol. Chem.* **252,** 3617–3625
28. Mourao, P. A., and Dietrich, C. P. (1979) Chondroitin sulfates of the epiphyseal cartilages of different mammals. *Comp. Biochem. Physiol. B Biochem. Mol. Biol.* **62,** 115–117
29. Wikstrom, B., Engfeldt, B., Heinegård, D., and Hjerpe, A. (1985) Proteoglycans and glycosaminoglycans in cartilage from the brachymorphic (bm/bm) mouse. *Collagen Relat. Res.* **5,** 193–204
30. Rosenberg, L. C., Tang, L. H., Choi, H. U., Pal, S., Johnson, T. L., Poole, A. R., Roughley, P. J., Reiner, A., and Pidoux, I. (1983) in *Limb development and regeneration* (Kelley, R. O., Goetinck, P. F., and MacCabe, J. A., eds) pp. 67–84, Alan R. Liss, New York
31. Hiraoka, S., Furuichi, T., Nishimura, G., Shibata, S., Yanagishita, M., Rimoin, D. L., Superti-Furga, A., Nikkels, P. G., Ogawa, M., Katsuyama, K., Toyoda, H., Kinoshita-Toyoda, A., Ishida, N., Isono, K., Sanai, Y., Cohn, D. H., Koseki, H., and Ikegawa, S. (2007) Nucleotide-sugar transporter SLC35D1 is critical to chondroitin sulfate synthesis in cartilage and skeletal development in mouse and human. *Nat. Med.* **13,** 1363–1367
32. Stanescu, V., Stanescu, R., and Maroteaux, P. (1984) Pathogenic mechanisms in osteochrondodysplasias. *J. Bone Jt. Surg.* **66,** 817–836
33. Fraser, R. D. (1958) Interpretation of infrared dichoism in axially oriented polymers. *J. Chem. Phys.* **28,** 1113–1115
34. Maroudas, A., and Evans, H. (1974) Sulfide diffusion and incorporation into human articularcartilage. *Biochim. Biophys. Acta* **338,** 265–279
35. Rossi, A., Bonaventure, J., Delezoide, A. L., Superti-Furga, A., and Cetta, G. (1997) Undersulfation of cartilage proteoglycans *ex vivo* and increased contribution of amino acid sulfur to sulfation *in vitro* in McAlister dysplasia/atelosteogenesis type 2. *Eur. J. Biochem.* **248,** 741–747
36. Pecora, F., Gualeni, B., Forlino, A., Superti-Furga, A., Tenni, R., Cetta, G., and Rossi, A. (2006) *In vivo* contribution of amino acid sulfur to cartilage proteoglycan sulfation. *Biochem. J.* **398,** 509–514
37. Ooira, A., Kimata, K., Suzuki, S., Takata, K., and Suzuki, I. (1974) A correlation between synthetic activities for matrix macromolecules and specific stages of cyto-differentiation in developing cartilage. *J. Biol. Chem.* **249,** 1637–1645
38. Dziewiatkowski, D. D. (1951) Radioautographic visualization of sulfur-35 disposition in the articular cartilage and bone of suckling rats following injection of labeled sodium sulfate. *J. Exp. Med.* **93,** 451–458
39. Dziewiatkowski, D. D. (1952) Radioautographic studies of sulfate-sulfur (^{35}S) metabolism in the articular cartilage and bone of suckling rats. *J. Exp. Med.* **95,** 489–496
40. Belanger, L. F. (1954) Autoradiographic visualization of the entry and transit of ^{35}S in cartilage, bone, and dentine of young rats and the effect of hyaluronidase *in vitro*. *Can. J. Biochem. Physiol.* **32,** 161–169
41. Hunziker, E. B., and Schenk, R. K. (1989) Physiological mechanisms adopted by chrondocytes in regulating longitudinal bone growth in rats. *J. Physiol.* **414,** 55–71
42. Wilsman, N. J., Farnum, C. E., Leiferman, E. M., Fry, M., and Barreto, C. (1996) Differential growth by growth plates as a function of multiple parameters of chondrocytic kinetics. *J. Orthop. Res.* **14,** 927–936
43. Buckwalter, J. A., Mower, D., Ungar, R., Schaeffer, J., and Ginsberg, B. (1986) Morphometric analysis of chrondrocyte hypertrophy. *J. Bone Jt. Surg. Am.* **68A,** 243–255
44. Bayliss, M. T., Osborne, D., Woodhouse, S., and Davidson, C. (1999) Sulfation of chondroitin sulfate in human articular cartilage. The effect of age, topographical position, and zone of cartilage on tissue composition. *J. Biol. Chem.* **274,** 15892–15900
45. Marcelino, J., Carpten, J. D., Suwairi, W. M., Gutierrez, O. M., Schwartz, S., Robbins, C., Sood, R., Makalowska, I., Baxevanis, A., Johnstone, B., Laxer, R. M., Zemel, L., Kim, C. A., Herd, J. K., Ihle, J., Williams, C., Johnson, M., Raman, V., Alonso, L. G., Brunoni, D., Gerstein, A., Papadopoulos, N., Bahabri, S. A., Trent, J. M., and Warman, M. L. (1999) CACP, encoding a secreted proteoglycan, is mutated in camptodactyly arthropathy-coxa vara-pericarditis syndrome. *Nat. Genet.* **23,** 319–322
46. Scheck, M., Parker, J., and Daentl, D. (1978) Hyaline cartilage changes in diastrophic dwarfism. *Virchows Arch. A Pathol. Anat. Histopathol.* **378,** 347–359
47. Shapiro, F. (1992) Light and electron microscopic abnormalities in diastrophic dysplasia growth cartilage. *Calcif. Tissue Int.* **51,** 324–331
48. Diab, M., Wu, J. J., Shapiro, F., and Eyre, D. (1994) Abnormality of type IX collagen in a patient with diastrophic dysplasia. *Am. J. Med. Genet.* **49,** 402–409
49. Stanescu, V., Do, T. P., Chaminade, F., Maroteaux, P., and Stanescu, R. (1994) Noncollagenous protein screening in the human chondrodysplasias. Link proteins, cartilage oligomeric matrix protein (COMP), and fibromodulin. *Am. J. Med. Genet.* **51,** 22–28
50. Ghadially, F. N. (1983) *Fine Structure of Synovial Joints*, Butterworths, London
51. Cortes, M., Baria, A. T., and Schwartz, N. B. (2009) Sulfation of chondroitin sulfate proteoglycans is necessary for proper Indian hedgehog signaling in the developing growth plate. *Development* **136,** 1697–1706
52. Sohaskey, M. L., Yu, J., Diaz, M. A., Plaas, A. H., and Harland, R. M. (2008) JAWS coordinates chondrogenesis and synovial joint positioning. *Development* **135,** 2215–2220
53. Gualeni, B., Facchini, M., De Leonardis, F., Tenni, R., Cetta, G., Viola, M., Passi, A., Superti-Furga, A., Forlino, A., and Rossi, A. (2010) Defective proteoglycan sulfation of the growth plate zones causes reduced chondrocyte proliferation via an altered Indian hedgehog signaling. *Matrix Biol.* **29,** 453–460
54. Kobayashi, T., Soegiarto, D. W., Yang, Y., Lanske, B., Schipani, E., McMahon, A. P., and Kronenberg, H. M. (2005) Indian hedgehog stimulates periarticular chondrocyte differentiation to regulate growth plate length independently of PTHrP. *J. Clin. Invest.* **115,** 1734–1742
55. Chen, X., Macica, C. M., Nasiri, A., and Broadus, A. E. (2008) Regulation of articular chondrocyte proliferation and differentiation by indian hedgehog and parathyroid hormone-related protein in mice. *Arthritis Rheum.* **58,** 3788–3797
56. Serizawa, S., Nagai, T., Ito, M., and Sato, Y. (1990) Cholesterol sulfate levels in the hair and nails of patients with recessive X-linked ichthyosis.

Clin. Exp. Dermatol. **15,** 13–15
57. Cohen, M. M. (2003) The hedgehog signaling network. *Am. J. Med. Genet. A* **123,** 5–28
58. Strott, C. A., and Higashi, Y. (2003) Cholesterol sulfate in human physiology. What's it all about? *J. Lipid Res.* **44,** 1268–1278
59. Ai, X., Do, A. T., Lozynska, O., Kusche-Gullberg, M., Lindahl, U., and Emerson, C. P., Jr. (2003) QSulf1 remodels the 6-*O*-sulfation states of cell surface heparan sulfate proteoglycans to promote Wnt signaling. *J. Cell Biol.* **162,** 341–351
60. Koziel, L., Kunath, M., Kelly, O. G., and Vortkamp, A. (2004) Ext1-dependent heparan sulfate regulates the range of Ihh signaling during endochondral ossification. *Dev. Cell* **6,** 801–813
61. Mohammadi, M., Olsen, S. K., and Ibrahimi, O. A. (2005) Structural basis for fibroblast growth factor receptor activation. *Cytokine Growth Factor Rev.* **16,** 107–137
62. Galante, L. L., and Schwarzbauer, J. E. (2007) Requirements for sulfate transport and the diastrophic dysplasia sulfate transporter in fibronectin matrix assembly. *J. Cell Biol.* **179,** 999–1009
63. Arrington, C. B., and Yost, H. J. (2009) Extra-embryonic syndecan 2 regulates organ primordia migration and fibrillogenesis throughout the zebrafish embryo. *Development* **136,** 3143–3152
64. Yamauchi, S., Hirahara, Y., Usui, H., Takeda, Y., Hoshino, M., Fukuta, M., Kimura, J. H., and Habuchi, O. (1999) Purification and characterization of chondroitin 4-sulfotransferase from the culture medium of a rat chondrosarcoma cell line. *J. Biol. Chem.* **274,** 2456–2463
65. Orellana, A., Hirschberg, C. B., Wei, Z., Swiedler, S. J., and Ishihara, M. (1994) Molecular cloning and expression of a glycosaminoglycan *N*-acetylglucosaminyl *N*-deacetylase/*N*-sulfotransferase from a heparin-producing cell line. *J. Biol. Chem.* **269,** 2270–2276
66. Habuchi, H., Habuchi, O., and Kimata, K. (1995) Purification and characterization of heparan sulfate 6-sulfotransferase from the culture medium of Chinese hamster ovary cells. *J. Biol. Chem.* **270,** 4172–4179
67. Myette, J. R., Shriver, Z., Liu, J., Venkataraman, G., Rosenberg, R., and Sasisekharan, R. (2002) Expression in *Escherichia coli*, purification and kinetic characterization of human heparan sulfate 3-*O*-sulfotransferase-1. *Biochem. Biophys. Res. Commun.* **290,** 1206–1213
68. Xu, D., Song, D., Pedersen, L. C., and Liu, J. (2007) Mutational study of heparan sulfate 2-*O*-sulfotransferase and chondroitin sulfate 2-*O*-sulfotransferase. *J. Biol. Chem.* **282,** 8356–8367
69. Kester, M. H., Kaptein, E., Roest, T. J., van Dijk, C. H., Tibboel, D., Meinl, W., Glatt, H., Coughtrie, M. W., and Visser, T. J. (2003) Characterization of rat iodothyronine sulfotransferases. *Am. J. Physiol. Endocrinol. Metab.* **285,** E592-E598
70. Carlsson, P., Presto, J., Spillmann, D., Lindahl, U., and Kjellén, L. (2008) Heparin/heparan sulfate biosynthesis. Processive formation of *N*-sulfated domains. *J. Biol. Chem.* **283,** 20008–20014
71. Tsang, K. Y., Chan, D., Cheslett, D., Chan, W. C., So, C. L., Melhado, I. G., Chan, T. W. Y., Kwan, K. M., Hunziker, E. B., Yamada, Y., Bateman, J. F., Cheung, K. M., and Cheah, K. S. E. (2007) Surviving endoplasmic reticulum stress is coupled to altered chrondrocyte differentiation and function. *PLoS Biol.* **5,** 568–585
72. Rajpar, M. H., McDermott, B., Kung, L., Eardley, R., Knowles, L., Heeran, M., Thornton, D. J., Wilson, R., Bateman, J. F., Poulsom, R., Arvan, P., Kadler, K. E., Briggs, M. D., and Boot-Handford, R. P. (2009) Targeted induction of endoplasmic reticulum stress induces cartilage pathology. *PLoS Genet.* **5,** e1000691
73. Tsang, K. Y., Chan, D., Bateman, J. F., and Cheah, K. S. (2010) *In vivo* cellular adaptation to ER stress. Survival strategies with double-edged consequences. *J. Cell Sci.* **123,** 2145–2154